Astronomy & Astrophysics manuscript no. output
May 11, 2020

Alone but not lonely: TESS and *Gaia* suggest binary interaction is always required to form hot subdwarf stars

Ingrid Pelisoli⋆, Joris Vos, Stephan Geier, Veronika Schaffenroth

Institut für Physik und Astronomie, Universität Potsdam, Haus 28, Karl-Liebknecht-Str. 24/25, D-14476 Potsdam-Golm, Germany

Received MONTH DD, YYYY; accepted MONTH DD, YYYY

ABSTRACT

Context. Hot subdwarfs are core-helium burning stars that show lower masses and higher temperatures than canonical horizontal branch stars. They are believed to be formed when a red giant suffers an extreme mass-loss episode. Binary interaction is suggested to be the main formation channel, but the high fraction of apparently single hot subdwarfs (up to 30%) has prompted single star formation scenarios to be proposed.
Aims. If hot subdwarfs could be formed as single, they would also be observed in non-interacting binaries. By studying hot subdwarfs in known wide binaries with main sequence companions and by seeking common proper motion pairs, we investigate the possibility that hot subdwarfs can form without interaction with a companion.
Methods. We have analysed light curves from the Transiting Exoplanet Survey Satellite (TESS) for all known hot subdwarfs showing composite spectra indicating the presence of a main sequence wide binary companion, probing for signs of previous interaction. To identify very wide binaries in common proper motion pairs, we have searched for companions to all known spectroscopically confirmed hot subdwarfs using *Gaia* DR2 astrometry.
Results. We find that most companions in composite hot subdwarfs show evidence of previous interaction in the form of mass and angular momentum accretion, resulting on short rotation periods whose distribution peaks at 2.5 days. We also report a shortage of hot subdwarfs with candidate common-proper motion companions.
Conclusions. We argue that the evidence of interaction in wide hot subdwarf binaries, combined with the shortage of common proper motion pairs that would be expected given their frequency among progenitors, suggests that binary interaction is always required for the formation of hot subdwarfs.

Key words. subdwarfs – binaries: wide – variables

1. Introduction

Hot subdwarf stars (sdO/Bs) are underluminous objects that lie in the extreme horizontal branch (EHB, Heber 1986). They have thinner hydrogen envelopes ($M_{\rm env} < 0.02\ M_{\odot}$) than canonical horizontal branch stars, being thus unable to sustain hydrogen shell burning. Because of their thin envelopes, they also appear hotter than their canonical counterparts. They show temperatures $T_{\rm eff} > 20\,000$ K and surface gravities in the range $4.5 < \log\ g < 6.5$ (for a complete review on sdO/Bs, see Heber 2016).

The characterisation of sdO/Bs is of interest for many fields of astronomy, from extragalactic to stellar astrophysics. In extragalactic astrophysics, they are known to account for a large fraction of the ultraviolet excess observed in early-type galaxies (O'Connell 1999). They contribute to Galactic astrophysics by allowing to probe the gravitational potential of the Milky Way, and in particular the mass of the dark matter halo (Tillich et al. 2011), because they can be among the fastest stars in the Galaxy (e.g. the hypervelocity star US708 in Geier et al. 2015). They can also show pulsations, being remarkable targets for asteroseismology and allowing to place constraints in stellar evolution theory (Charpinet et al. 2009). sdO/Bs in close binaries can qualify as type Ia supernova progenitors (e.g. Maxted et al. 2000) and/or verification sources for future space-based gravitational wave detectors such as the Laser Interferometer Space Antenna (*LISA*, Kupfer et al. 2018).

Despite their ubiquitous importance in astronomy, their formation remains puzzling. The consensus is that hot subdwarfs are the progeny of low- to intermediate-mass stars that have undergone an episode of enhanced mass-loss at the tip of the red-giant branch (RGB). Binary interaction is the main evoked explanation for such an episode.

Three main binary evolution scenarios have been described in detail by Han et al. (2002, 2003): (i) common envelope evolution, (ii) stable Roche-lobe overflow (RLOF), and (iii) the merger of two He white dwarfs. In scenario (i) the more massive star in the binary would evolve to the RGB and fill its Roche lobe, transferring mass to the companion inefficiently, leading to the formation of a common envelope that is eventually ejected, leaving an exposed He-burning core in a close binary (orbital period of up to a few days). If the mass transfer is instead stable (scenario ii), the outer layers of the sdO/B progenitor are slowly stripped away by its companion. This channel leads to the formation of sdO/Bs with main sequence companions in wide binaries (orbital periods of tens to hundreds of days).

Supporting these two channels, a large fraction of sdO/Bs is found in binaries. About one-third are found in close binaries with periods from hours to a few days consistent with scenario (i), mostly showing white dwarf or M-type main sequence stars as companions (Maxted et al. 2001; Morales-Rueda et al. 2003; Geier et al. 2011b; Copperwheat et al. 2011), whereas 30–40% show composite-colours and/or spectra indicating the presence of K to F type companions in wide orbits (Stark & Wade 2003).

⋆ pelisoli@astro.physik.uni-potsdam.de

The latter are often referred to as composite hot subdwarfs (Vos et al. 2018a).

It should be noted that the large observed fraction of composite binaries is not necessarily an indication of a previous mass-transfer phase forming the hot subdwarf. Given evolutionary timescales and the age of the Universe, sdO/B progenitors descend from main sequence stars of type F or earlier, which have binary fractions $\gtrsim 50\%$ (e.g. Duchêne & Kraus 2013). Therefore a similar fraction of hot subdwarfs in composite binaries could be expected, even without any previous interaction.

A first attempt to check whether the visible companions in composite sdO/B systems were sufficiently close to support previous interaction was made by Heber et al. (2002), who tried to resolve 19 composite systems with the Hubble Space Telescope. Considering the observed separation distribution of progenitors in binary systems, about one third of the observed sample should have been resolved. However, only two systems were resolved, one of which turned out be a hierarchical triple system with the sdB being part of a close, single-lined binary.

Although this result already indicated a significant deviation of the separation distribution of composite hot subdwarfs from their progenitor systems, the stable RLOF-channel could only be finally proven when the first orbital solutions of composite sdB systems were determined (Deca et al. 2012; Barlow et al. 2012, 2013; Vos et al. 2012, 2013). The derived long periods also required an update of the binary evolution models to be consistent with observations (Chen et al. 2013). A dedicated survey of a small sample of composite systems bright enough to be observed with high-resolution spectrographs showed that a high fraction of systems shows radial velocity variability and, importantly, high values of $v \sin i$ (> 10 km/s) for the companions, suggesting a high rate of previous interactions (Vos et al. 2018a).

On the other hand, for a large fraction of sdO/Bs, of up to 30%, no companions have been found. This fraction is even much higher for the sdO/B stars found in globular clusters (see Latour et al. 2018, and references therein). In the binary framework, those single objects are mainly explained as the result of the remaining scenario: a merger of two He white dwarfs. In fact a few single sdO/Bs are found to be fast rotators, supporting this theory (e.g. EC 22081-1916 and SB290 in Geier et al. 2011a, 2013, respectively). However, most of the single sdBs have been found to be very slow rotators both from analyses of the rotational line broadening (Geier & Heber 2012) and from asteroseismic analyses of space-based light curves (Baran et al. 2009, 2012; Pablo et al. 2012; Reed et al. 2014). In addition, the agreement between model predictions and observations is still poor (Zhang et al. 2009), and the predicted broad mass distribution of systems resulting from mergers seems to be at odds with the observed narrow distribution (Schneider et al. 2019). Moreover, the companions of helium white dwarfs are found to be mostly canonical to massive white dwarfs (Brown et al. 2020), suggesting a shortage of progenitors for the merger scenario.

Alternative formation scenarios relying on single star evolution have been proposed. D'Cruz et al. (1996) proposed that strong stellar wind mass loss in the RGB phase could place some objects in the EHB. Sweigart (1997) suggested that helium mixing from the hydrogen shell into the envelope, driven by internal rotation, could cause enhanced mass-loss in the RGB. However, if these single evolution scenarios were indeed possible, there must also be sdO/Bs in wide binaries that have undergone no interaction. In these systems, neither of the components should show any measurable traces of previous interactions, such as increased rotation rates due to transfer of angular momentum observed in the confirmed RLOF systems (Vos et al. 2018a) or pollution due to accreted matter. In particular, given the properties of the progenitor systems (e.g. De Rosa et al. 2014; Moe & Di Stefano 2017; El-Badry & Rix 2019), there must be a significant fraction of very wide, resolved visual binaries observable as common proper motion pairs.

In this work, we investigate the possibility that sdO/Bs could form without binary interaction by (i) characterising rotation rates for the companions in known composite binaries and (ii) searching for common proper motion companions to all spectroscopically confirmed sdO/Bs. In Section 2, we analyse light curves from the Transiting Exoplanet Survey Satellite (TESS) for known sdO/Bs in composite binaries in search for evidence of mass transfer. Mass transfer causes angular momentum to be gained by the companion stars, which are thus predicted to spin-up (e.g. Kippenhahn & Meyer-Hofmeister 1977; Popham & Narayan 1991). In Section 3, we perform a search for common proper motion companions to sdO/Bs with distances up to 20 000 AU ($\approx$ 0.1 pc), where no interaction is expected. We present a discussion of our results in Section 4, and conclude in Section 5.

2. TESS light curves for composite hot subdwarfs

The TESS mission (Ricker et al. 2015) was launched in 2018 to obtain high-precision photometry from space with the goal of finding nearby rocky exoplanets. The nominal two-year mission will observe 26 sky sectors, each with a field of $24^\circ \times 90^\circ$, for 27 days. The sectors cover over 90% of the sky, avoiding only a narrow band around the ecliptic already partially explored by the K2 mission (Howell et al. 2014). There is overlap between different sectors, therefore the total coverage can be much larger than 27 days (up to 351 days for stars around both ecliptic poles). TESS obtains images of observed sectors every 2 seconds, which are used for guiding. These 2 second images are stacked into 20 seconds, 2 minutes, or 30 minute cadence images that can be downloaded to the ground. The 20 second cadence postage-stamps are only downloaded for a small number of very bright asteroseismology targets, whereas 2 minute postage-stamps are obtained for a large number of objects proposed by the community. Finally, every pixel observed by TESS will be downloaded at 30 minute cadence.

Although TESS is designed as an exoplanet mission, the cadence and high precision are also of particular interest for studying binary stars and intrinsic stellar variability. For evolved compact stars such as hot subdwarfs and also white dwarfs, the TESS Asteroseismic Science Consortium (TASC) Working Group 8 (WG8) has proposed an extensive variability survey including all known evolved compact stars brighter than 16th magnitude. Up to Sector 20, 1125 hot subdwarf and candidates from the catalogues of Geier et al. (2017) and Geier et al. (2019) have been observed with 2 minute cadence.

The catalogue of spectroscopically confirmed hot subdwarfs from Geier et al. (2017) has recently been updated taking into account input from the *Gaia* data release 2 (DR2, Gaia Collaboration et al. 2018), as well as the latest releases of the Large sky Area Multi-Object fiber Spectroscopic Telescope (LAMOST Zhao et al. 2012). We have crossmatched the updated catalogue (Geier 2020) with the list of observed stars from the TASC WG8. We identified 156 stars classified as composite hot subdwarfs with main sequence companions (sdO/B + MS, + A, + F, + G, + K) observed up to Sector 20. To remove objects that might not be real binaries, but rather have been misclassified due to contamination by a nearby star, we excluded objects with another

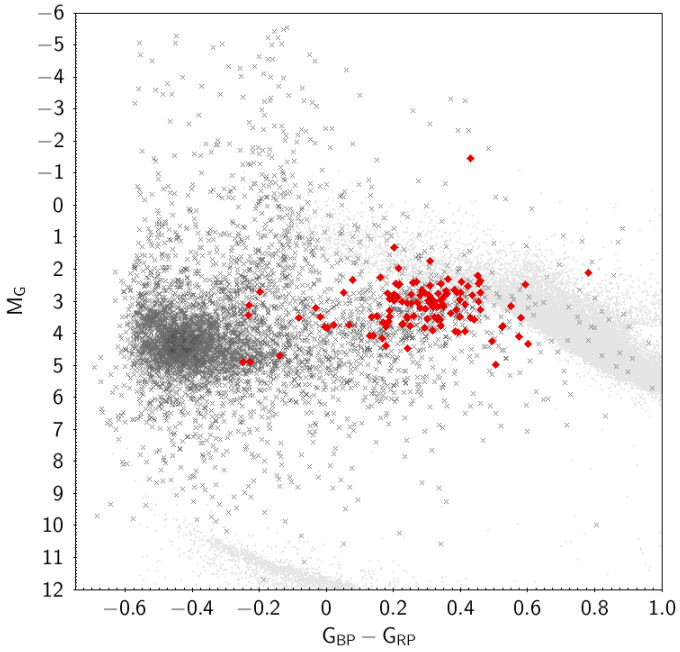

Fig. 1. Colour-magnitude diagram showing all stars from the catalogue of Geier (2020) as grey crosses. The composite systems analysed in this work are shown as red diamonds. At this point, no quality cuts have been performed in the astrometry, which explains the high spread. Sample C of Lindegren et al. (2018) is shown in the background to facilitate the location of the main sequence and other evolutionary stages.

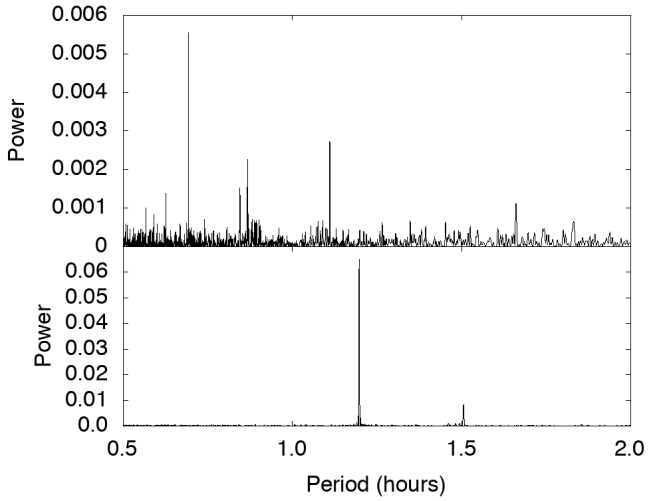

Fig. 2. TIC 71013467 (top) and TIC 158235404 (bottom), two new pulsators that are part of our sample. They show periods in the range of 45 min to 2 hours, typical of g-mode hot subdwarf pulsators (Green et al. 2003).

source in *Gaia* DR2 within 5 arcsec, unless they were confirmed radial velocity variables. We also excluded objects classified as close binaries in the literature, as well as objects whose fit to the spectral energy distribution (SED) indicated they were actually single stars. We were then left with 123 composite hot subdwarfs observed with TESS (Fig. 1).

We have searched for variability in the light curves of all 123 composite objects using a Lomb-Scargle periodogram (Lomb 1976; Scargle 1982). We have used the light curves made available by the TESS Science Processing Operations Center (SPOC), and specifically the PDCSAP flux, which corrects the simple aperture photometry (SAP) to remove instrumental trends, as well as contributions to the aperture expected to come from neighbouring stars other than the target of interest given a pre-search data conditioning (PDC). This is particularly relevant for TESS, because the pixel size is nearly 21". The pipeline also provides an estimate of how much of the flux in the aperture belongs to the target systems in the `CROWDSAP` parameter. To avoid possible zero-point inconsistencies between different sectors, the reported fluxes were divided by the mean flux in each sector for each star. We have also performed sigma-clipping to exclude any measurements more than 5-sigma away from the mean value.

Our initial analysis consisted of calculating the periodogram up to the Nyquist frequency, with sampling to give ten points per significant periodogram peak, phase-folding the data to the dominant peak, and inspecting the periodogram and phase-folded light curve to confirm any variability. We have found 90 out of the 123 stars (73%) to show variability. The false-alarm probability (FAP) of the dominant period for objects classified as variable was in most cases FAP $\lesssim 10^{-20}$. For two objects, the periodogram is typical of g-mode hot subdwarf pulsators (Green et al. 2003), as shown in Fig. 2. Both of these are new discoveries; the identified periods are listed in Table A.1.

For the remaining objects, the variability cannot be attributed to pulsations of the hot subdwarf star. It instead likely originates in the main sequence companion. One possible scenario is an interplay between stellar activity and rotation, as seen for many Kepler (e.g. Reinhold & Gizon 2015) and K2 objects (e.g. Reinhold & Hekker 2020). The activity causes temperature and therefore brightness changes across the surface of the star, which are seen as periodic variability as the star rotates. To test whether that was the cause of the variability, we have analysed the light curves for these 90 variable objects following the approach of Reinhold & Reiners (2013), as summarised below.

Firstly, a Lomb-Scargle periodogram is calculated up to the Nyquist frequency. We have set the minimal frequency to $2/T$, where T is the duration of the light curve. This assumes that a minimum of two cycles are necessary to detect the variability. As above, we used an oversampling factor of ten to determine the frequency step, i.e. $\delta f = 1/(10T)$. Once the dominant peak was identified, we have performed pre-whitening to identify a second possible peak. Computing a Lomb-Scargle periodogram is equivalent to fitting a sine wave to the data, hence the pre-whitening consists on simply subtracting the fitted sine wave from the data, and computing the periodogram of the residuals. As we are only interested in the dominant period and not in all observed periods, this process has been performed only once.

The main goal of the pre-whitening was to verify that the dominant period was not an alias. In some cases spots can be located on opposite sides of the star, in which case the dominant peak will actually correspond to half the rotation period. Following the prescription of Reinhold & Reiners (2013), we have compared the two periods with largest power in the periodogram and, if the difference between twice the first period and the second period was less than 5%, we selected the longer one, which is more likely the correct period.

For many stars, differential rotation is present, in which case a second dominant peak which is not an alias is detected. To identify this, we checked whether the period P_2 was within 30% of P_1 (which suggests it is consistent with differential rotation, Reinhold & Reiners 2013). Defining $\alpha = |P_2 - P_1|/\max(P_1, P_2)$, we verified if P_2 was such that $\delta f < \alpha < 0.3$, where the lower limit accounts for the frequency resolution of each light curve

of $1/(10T)$. If α was within these limits, P_2 was accepted as a second significant period arising from differential rotation, otherwise it was discarded. This step was performed to improve precision on P_1, since the second sine wave with period P_2 can have a significant effect on the light curve. Last, sine parameters for both P_1 and P_2, when significant, were used as input for a global sine fit, summing both sine waves and allowing for both periods to vary. We show two examples in Fig. 3.

Finally, to identify stars whose cause of variability is possibly not rotation, we compared the number of zero crossings with the predicted one for a sine wave. A single sine wave has two zero crossings per period, therefore the observed period is indeed due to rotation we should expect a number of crossings of the order of $N = T \times 2/P_1$. A number of crossings higher than that hints at a different cause for variability, such as stellar pulsations or irregular variations. We estimated the number of zero crossings by smoothing the data using a boxcar average with a width of $5\times P_1$, followed by an average every ten points to reduce fluctuations due to uncertainty in flux. The number of crossings was not used as a hard-limit, given that more crossings can be shown if e.g. there are spots on opposite sides of the star, or if the rotation pattern exhibits double dips (as seen predominantly for slow rotators, Basri & Nguyen 2018).

We instead further inspected objects showing more than two crossings per period. Many of those had already been flagged as uncertain during our initial inspection, for being only marginally significant or showing large spreading. An example is shown in Fig. 4. Other objects not previously flagged showed higher number of crossings mainly because of fluctuations due to the uncertainty in flux. We further flagged as uncertain three objects showing a number of crossings lower than predicted that clustered closely to the two identified pulsators (see Fig. 5). We were then left with 61 composite systems whose variability we interpret as due to rotation, listed in Table 1. The remaining 29 variable objects are listed in Table 2, whereas objects not observed to vary (NOV) are listed in Table 3 with the respective detection limits.

Figure 6 shows, in black, the histogram of the obtained periods for the 61 presumably rotational variables. The mean period is 2.5 days, with a one-sigma spread of 1.4 days. To obtain a comparison with main sequence stars with no hot subdwarf companions, we have used the data from Reinhold & Gizon (2015), who determined the rotational periods for more than 18 500 stars observed by the Kepler mission. To account for the temperature distribution of our sample, as well as for the fact that we can only detect periods shorter than about 13.5 days for most objects (which were only observed during one sector), we selected for each object in our sample the stars in Reinhold & Gizon (2015) with same effective temperature (within 5%).

The temperature for the main sequence stars in the systems in our sample was determined with a multi-component fit to the spectral energy distribution (SED), taking into account both the contribution of the hot subdwarf and of the companion. The SED fitting procedure uses literature photometry from APASS (Henden et al. 2015), 2MASS (Skrutskie et al. 2006), WISE (Cutri & et al. 2012), and *Gaia* (Gaia Collaboration et al. 2018; Riello et al. 2018; Evans et al. 2018), and is constrained by the reddening obtained from the dust maps of Lallement et al. (2019) and the *Gaia* parallax. To model the SED, Tübingen NLTE Model-Atmosphere package models (Werner et al. 2003) and Kurucz atmosphere models (Kurucz 1979) are used for respectively the hot subdwarf star and the cool companion. A more detailed description of the SED fitting procedure is given in Vos et al. (2017, 2018b).

Next, given a sample of stars with consistent temperature for each of our objects, we randomly selected the period of one of the stars in the comparison sample, considering only periods within our detectable range (we assumed that periods shorter than the maximum period in our sample, of $\simeq$ 7.5 days, could be detected). We repeated this a hundred times, obtaining thus one period histogram for each realisation. We then calculated the mean histogram, as well as an uncertainty given by the standard deviation. This histogram is shown in blue in Figure 6.

The period distribution for main sequence companions to hot subdwarfs is clearly different from the distribution of canonical main sequence stars. This is confirmed by a two-sample Anderson-Darling test, which suggests that the null hypothesis that these two distributions are sampled from the same population can be safely rejected (p-value < 0.001).

Performing a similar comparison for the amplitudes results in Figure 7. To avoid differences due to variable precision in different magnitude ranges, in this case we have also constrained the comparison sample to have a similar magnitude distribution to our observed sample, by drawing comparison objects with magnitudes within 5% of the value for each of our systems (or within 10% when no pair was found). Albeit more subtle for the amplitude distribution compared to the period distribution, a two-sample Anderson-Darling test confirms that the behaviour of the companion stars also does not follow the trend of canonical stars (p-value < 0.001).

Figures 6 and 7 suggest that main sequence stars with a subdwarf companion show, in average, shorter periods and lower amplitudes than the bulk of main sequence stars. Stellar activity is found to decrease with age (e.g. Davenport et al. 2019), therefore this difference in amplitude suggests that the composite companions are older than the main sequence stars in the comparison sample. This is expected, given that the low-mass progenitors of the hot subdwarfs already evolved beyond the RGB and their companions should have the same age, whereas the main sequence stars from Reinhold & Gizon (2015) should show a large spread in age and include young sytems.

The short rotation periods of the main sequence stars in the composite systems, which are usually characteristic of young and early-type stars, can be explained by accretion. As the hot subdwarf progenitor reaches the red giant phase and fills its Roche-lobe, the companion will accrete mass and be spun-up to nearly break-up, before starting to spin down again. The short periods can therefore be interpreted as evidence for interaction in these wide (orbital periods $\gtrsim$ 500 days) binaries.

3. *Gaia* DR2 search for common proper motion

One of the many applications of the unprecedented *Gaia* DR2 is the search for common proper motion pairs (e.g. El-Badry & Rix 2018; Fouesneau et al. 2019). Whereas close binaries (separations $\lesssim$ 20 mas) are not resolved by *Gaia*, wider binaries can be identified as co-moving pairs thanks to the precise *Gaia* astrometry. For hot subdwarfs, radial velocity variability has been used as the main indicator for binarity, which limits the detection to objects with periods of a few tens of years at best (the discovery of hot subdwarfs dates back to the 1950s with Humason & Zwicky 1947, although their evolutionary origin was only understood much later). This is equivalent to separations smaller than $\simeq$ 20 au, or $\simeq$ 20 mas at a distance of 1 kpc, coinciding with objects unresolved by *Gaia*.

Gaia therefore opens a new window to study hot subdwarf binarity by allowing for the first time to seek binary companions beyond 20 au. We have performed a search for common

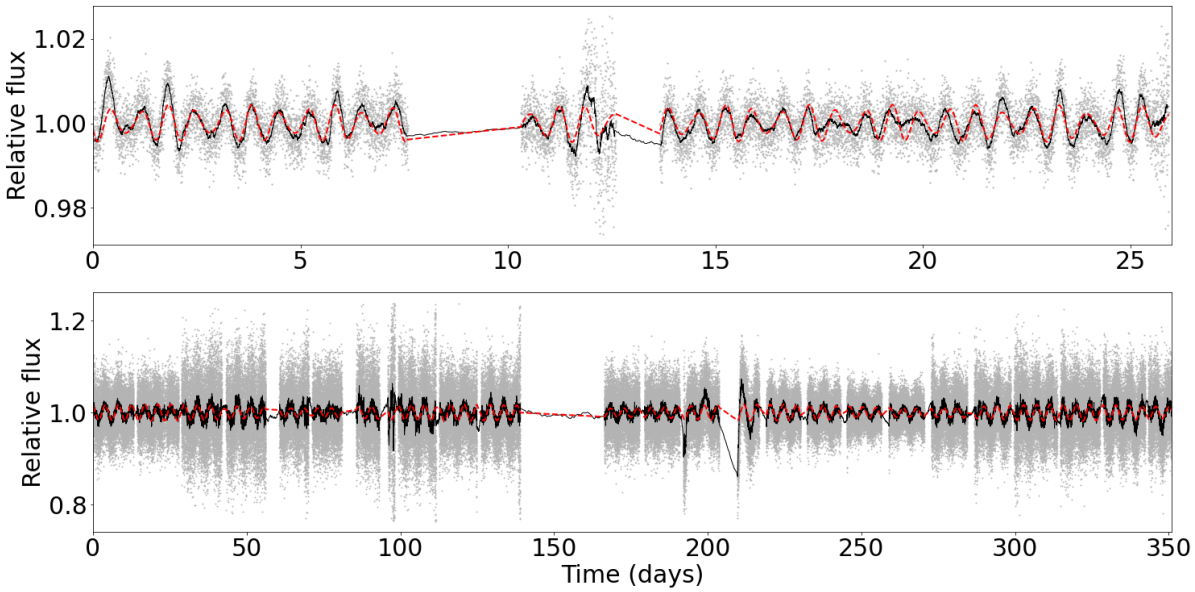

Fig. 3. TIC 12528447 (top) and TIC 382518318 (bottom), two systems for which the variability has been attributed to rotation of the main sequence companion. The former was observed in only one sector, while the latter is in the TESS continuous viewing zone and has 2 min cadence data for 12 sectors. The grey dots are the TESS data, the black line is a running mean every 50 points, and the dashed red line is the multi-component fit.

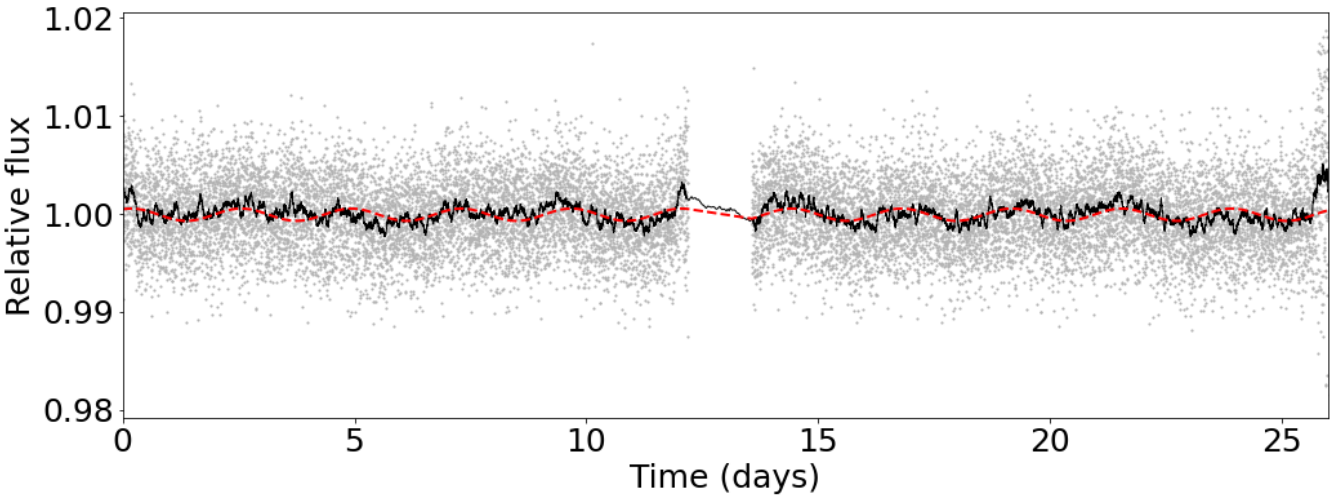

Fig. 4. TIC 13069774, a variable star showing a number of crossings more than twice the predicted value for sinusoidal variation.

proper motion companions to spectroscopically confirmed hot subdwarfs in the catalogue of Geier (2020). We followed the approach of Fouesneau et al. (2019), and searched for co-moving sources with proper motions consistent with those of the hot subdwarfs and candidates within 3 σ according to:

$$\frac{((\mu_\alpha)_{\rm SD} - (\mu_\alpha)_{Gaia})^2}{(\sigma_{\mu,\alpha})^2_{\rm SD} + (\sigma_{\mu,\alpha})^2_{Gaia}} + \frac{((\mu_\delta)_{\rm SD} - (\mu_\delta)_{Gaia})^2}{(\sigma_{\mu,\delta})^2_{\rm SD} + (\sigma_{\mu,\delta})^2_{Gaia}} \leq (3\ {\rm mas/yr})^2 \quad (1)$$

where μ_α is the proper motion in right ascension (α), μ_δ is the proper motion in declination (δ), $\sigma_{\mu,\alpha}$ is the uncertainty in μ_α, and $\sigma_{\mu,\delta}$ is the uncertainty in μ_δ. The subscripts 'SD' and '*Gaia*' refer to the queried hot subdwarfs, and to objects in the *Gaia* catalogue other than the hot subdwarf. Similarly, we have also restricted the parallax (ϖ) difference between the two sources to 3 sigma:

$$\frac{(\varpi_{\rm SD} - \varpi_{Gaia})^2}{(\sigma_\varpi)^2_{\rm SD} + (\sigma_\varpi)^2_{Gaia}} \leq (3\ {\rm mas})^2 \quad (2)$$

Finally, we have only considered *Gaia* sources whose projected separation was smaller than 20 000 AU ($\sim$ 0.1 pc), because pairs with larger separations are likely to be eventually disrupted by external gravitational perturbations (Retterer & King 1982; Weinberg et al. 1987). This also helps limiting the contamination by chance alignments, which grows rapidly at large separations (Andrews et al. 2017). The ADQL query applying these conditions can be found in Appendix B.

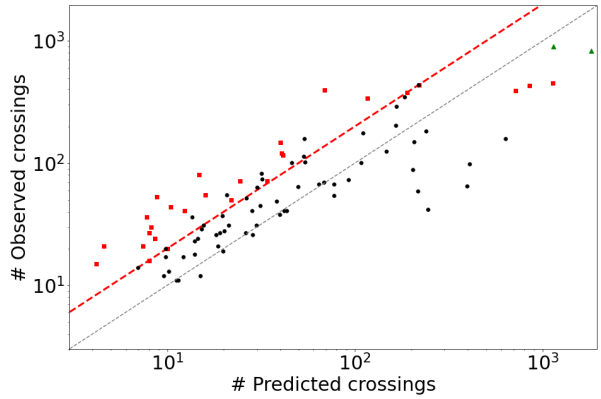

Fig. 5. Observed number of zero crossings as a function of the predicted number of crossings for all 90 variables. The two g-mode hot subdwarf pulsators are shown as green triangles. The two dashed lines represent equality (bottom, in grey) and observed number of crossings equal to twice the number of predicted crossings (top, in red). Object not included as rotational variables are shown as red squares. Objects with a high number of predicted crossings due to showing short periods often show less observed crossings because TESS data is not continuous, presenting a gap every $\simeq$ 13 days when data is transmitted to Earth.

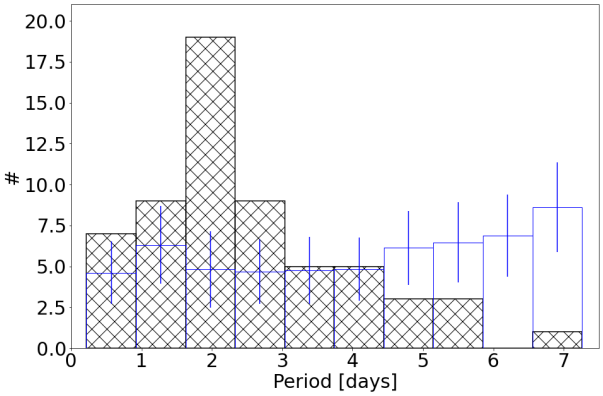

Fig. 6. Number histogram of the obtained rotational periods for the hot subdwarf companions (black, hatched). As a comparison, we show a number histogram obtained from drawing a sample of objects from Reinhold & Gizon (2015) with the same temperature distribution as our sample and periods within the detectable range (in blue). This was repeated a hundred times; the height of the histogram is the average over all realisations, whereas the error bar is the standard deviation.

The query returned 299 matches for 237 stars. We next applied quality filters to the astrometry of both hot subdwarf and candidate companion, by selecting only objects with parallax uncertainties smaller than 20%, and applying the quality filters of Lindegren et al. (2018), i.e.

$$1.0 + 0.015\,(G_{BP} - G_{RP})^2 < E < 1.3 + 0.06\,(G_{BP} - G_{RP})^2 \quad (3)$$

where E is the `phot_bp_rp_excess_noise`, the photometric excess factor obtained by comparing fluxes in the G_{BP} and G_{RP} passbands to the total G flux, and

$$u < 1.2\,\mathtt{max}(1, \exp(-0.2(G - 19.5))) \quad (4)$$

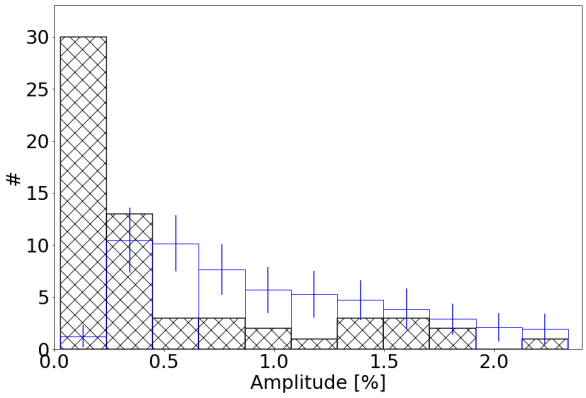

Fig. 7. Same as Figure 6, but for the detected amplitude of variability.

where

$$u = \sqrt{\frac{\mathtt{astrometric\_chi2\_al}}{(\mathtt{astrometric\_n\_good\_obs\_al} - 5)}}$$

with `astrometric_chi2_al` being the value of the chi-square statistic of the astrometric solution, and `astrometric_n_good_obs_al` being the number of good observations; both are given in the *Gaia* DR2 table.

This results on 16 common proper motion candidates, listed in Table 4. The comparison between *Gaia* measurements for the pairs is shown in Fig. 8. Figure 9 illustrates the position of both the hot subdwarfs and their candidate companions in a colour-magnitude diagram. We provide more details of each of these hot subdwarfs in Section 3.1.

Given the number of hot subdwarfs with good astrometry (Eqs. 3 and 4), even if all our identifications are confirmed as hot subdwarfs with a common proper motion pair, this implies a fraction of only $\simeq$ 0.5%. Note that this fraction refers to the inhomogeneous sample of spectroscopically classified hot subdwarfs, and cannot be generalised given that no selection effects are taken into account. Yet, this very small incidence of common proper motion pairs among confirmed hot subdwarfs suggests that such systems are much less common than for their progenitors.

3.1. Hot subdwarfs with candidate common proper motion companions

The 16 objects in the hot subdwarf catalogue of Geier (2020) with identified possible common proper motion companions are described in more detail below. We refer to the objects using the *Gaia* DR2 source id, but also include their identification as in Geier (2020) for readability.

312628749626419328 (GALEX J01012+3125): it is classified as sdB+MS in Geier (2020). The available LAMOST spectra show instead a single sdB, and the *Gaia* $G_{BP} - G_{RP}$ colour of -0.37 also suggests there is no composite companion. The classification might rely on photometry that could have been contaminated by the common proper motion companion, which is 6.8" away. There is, on the other hand, a shift of 37 $\pm$ 2 km/s between LAMOST spectra taken 678 days apart, which cannot be explained by the common proper motion companion.

601188910547673728 (LAMOST J082517.99+113106.3): also classified as sdB+MS (Geier 2020), but in this case the clas-

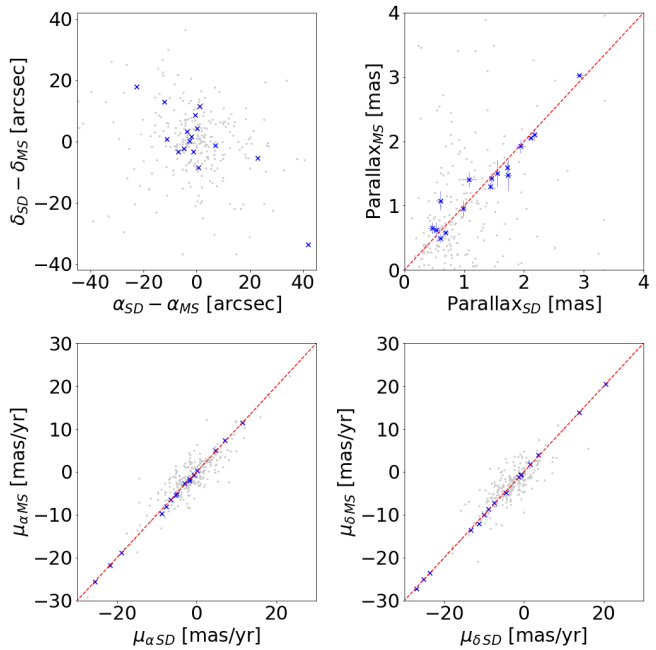

Fig. 8. Comparison between parameters for all matches (grey), and only those with good astrometry (blue). The top left panel shows the difference between coordinates of the hot subdwarf and the candidate companion. The top right panel compares the parallax of the two objects, whereas the bottom panels compare each component of the proper motion. The dashed lines represent equality.

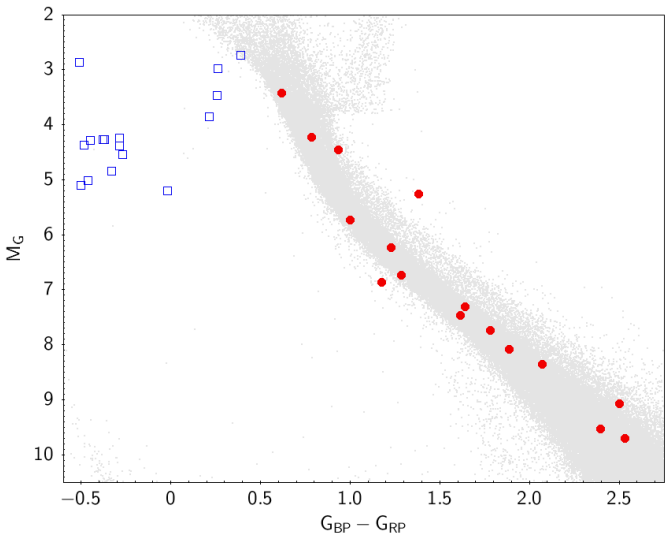

Fig. 9. Colour-magnitude diagram showing the position of all hot subdwarf stars that have a common proper motion pair candidate. The hot subdwarfs are shown as open blue squares, and the candidate companions are shown as filled red circles. Grey is the same as in Fig. 1.

sification would seem to be confirmed at first glance by the available LAMOST spectrum. However, the size of the LAMOST fibres of 3.3" means that the common proper motion companion, which is only 2.7" away and has similar brightness, contaminates the spectrum.

992534888766785024 (GALEX J063952.00+515658.00): it is classified as a single sdB (Geier 2020), but Németh et al. (2012) suggest it could be a close binary because of the large radial velocity (> 100 km/s) with respect to the kinematic local standard of rest (LSR).

1332156747638095488 (PG 1623+386): classified as sdOB (Geier 2020), it has been flagged as a visual double by Saffer et al. (1998), likely because of the common proper motion pair at a distance of 4.1".

1883850072814402048 (GALEX J22484+2714): the literature on this object is scarce; it has only been included in the catalogues of Geier et al. (2019) and Geier (2020) as sdB+MS. The brightness (G = 13.4) and relative red colour ($G_{BP} - G_{RP}$ = 0.26) suggest it might be instead a misclassified blue horizontal branch (BHB) star. Note that the companion is almost 40" away, and therefore should not contaminate the *Gaia* colour.

2103959862471941632 (Kepler J19028+4134): this star has been observed by the Kepler mission. Whereas Østensen et al. (2010) reported no pulsations compatible with a hot subdwarf, McNamara et al. (2012) identified a peak at 0.21 cycles/day with an amplitude of 0.0194%, and classified the object as a possible slowly-rotating B star. However, *Gaia* places this object within the hot subdwarf cloud (M_G = 9.7, $G_{BP} - G_{RP}$ = −0.46), which suggests that the variability has instead another origin, likely related to a binary companion other than the common proper motion pair, since such period is not expected to be observed in a single hot subdwarf or due to a distant (θ = 16") companion.

3484319745326973824 (EC 11429-2701): this object has also been observed by TESS (TIC 32661254) and was included in our analysis of Section 2. It was observed and classified as part of the Edinburgh-Cape Blue Object Survey (EC Survey, Kilkenny et al. 1997), and our SED fit indicates the presence of a composite companion with $T_{\rm eff} \simeq 6400$ K. The common proper motion companion is 6.44" away, is five magnitudes fainter than the hot subdwarf, and has its own photometry measurements in VizieR, therefore it should not have affected our SED fit. This is thus likely a triple system, with an inner unresolved binary.

3868418219635118080 (GALEX J11009+1055): it has been classified as a composite hot subdwarf by Németh et al. (2012), with a F6V type companion showing $T_{\rm eff} \approx 6430$ K. Given that the common proper motion companion is resolved and more than 8.5" away, it is rather unlikely that it contaminated the spectrum. Moreover, the *Gaia* DR2 archive suggests a $T_{\rm eff} = 4750^{+245}_{-128}$ K and $R = 0.578^{+0.032}_{-0.027}\ R_\odot$ for the common proper motion companion, which is more compatible with a late-G or early-K main sequence star. Therefore this is possibly a hierarchical triple system.

4877263019073081600 (EC 05015-2831): it is a known composite system that has also been included in the analysis of Section 2 (TIC 13069774, shown in Fig. 4). The common proper motion companion is at almost 21" away, having no contribution to the SED. This is another triple candidate.

1429755412672689536 (PG 1618+562): although it is classified as sdBV+F3 in Geier (2020), Drilling et al. (2013) include this object as a single sdB reference star. The colour-excess which lead to the composite classification is actually due to the common proper motion companion at 3.6", which was previously identified by Silvotti et al. (2000).

For the remaining systems (1659750327258228352 = PG 1411+590; 1660055029417965952 = GALEX J14085+5940; 1891098500140100352 = FBS 2253+335; 2002880555945732992 = KPD 2254+5444; 3381286602335612416 = LAMOST J065446.63+244926.8; 4491274930955326080 = SDSS J172125.76+090311.2), the literature refers mostly to their inclusion in hot subdwarf

catalogues, with no study on their binarity to the best of our knowledge.

4. Discussion

We find that a large fraction of composite hot subdwarf binaries present evidence for interaction in the form of accretion, with 61 of the 123 analysed systems showing variability consistent with rotation of the companion. The rotation periods shown by the main sequence companions are significantly smaller than those shown by a comparison sample of main sequence stars.

The observed periods can be well described by a log-normal distribution with mean $\log P$[days] = 0.35 and standard deviation $\log P$[days] = 0.27. The period distribution for main sequence stars in Reinhold & Gizon (2015) within the temperature range of the our sample can be described by a log-normal distribution with mean $\log P$[days] = 1.19 and standard deviation $\log P$[days] = 0.26. The distributions show therefore the same width, but the mean is shifted towards much lower values for the hot subdwarf companions. The longest period in our sample has about 10% chance of coming from the distribution with larger mean, with all other periods showing probabilities lower than 5%. However, we see no evidence for bi-modality in our sample, and a Shapiro-Wilk test cannot reject the null hypothesis that the logarithms of the observed periods follow a normal distribution (assuming a confidence level of 99%), therefore we interpret all observed periods to come from the same distribution.

The observed amplitudes are also found to be significantly lower than for the comparison sample. Older stars show lower amplitudes, therefore this suggests that these companion stars are older than the stars in the comparison sample. Although they are rejuvenated by accretion, which explains their short orbital periods, the accretion would not affect their interiors significantly (given that accretion rates are fairly small, Toonen et al. 2012; Vos et al. 2020), hence their level of activity is unaffected and the amplitudes remain low. In other words, these stars appear young if their rotational periods are considered, but the amplitudes reveal them to be old.

For further 29 stars, variability is detected, but cannot be safely attributed to rotation. These objects seem to be an unremarkable subsample of the complete sample of 123 composite systems, with G magnitude, CROWDSAP, number of observed sectors, and effective temperature of the companion all similarly distributed to the entire sample, as shown in Fig. 10. This is also indicated by two-sample KS tests, in which the null hypothesis that the parameters for these 29 stars are drawn from the same population as the parameters for the whole sample of 123 objects cannot be rejected. Therefore we remove these objects from our sample, with the exception of the systems for which only the pulsation of the subdwarf is detected, but no rotation of the companion even after pre-whitening is performed. This effectively reduces our sample to 96 systems, out of which 35 show no observed variability due to rotation, and 61 show variability consistent with rotation spun-up by accretion. Considering this sample, the fraction of composite systems with evidence for accretion is $63.5^{+4.6}_{-5.1}$%, where the uncertainties were calculated assuming a binomial distribution given the low-number statistics (see e.g. Burgasser et al. 2003) and indicate the 68% confidence level interval.

However, it is important to notice that the probability of detection of variability is not homogeneous throughout the sample. The NOV systems are, on average, fainter than the systems for which rotational variability has been detected (median G = 13.4 for rotational variables, compared to G = 14.6 for NOV systems). They are also in fields showing larger crowding, with the median of CROWDSAP being equal to 0.97 for rotational variables, but 0.89 for NOV systems. Furthermore, most of the NOV systems have data in only one sector (29 out of 33, 88%), while almost 30% of the rotational variables have data in more than one sector. This implies that the detection power is smaller for the systems in which no variability has been detected, compared to those with observed variability.

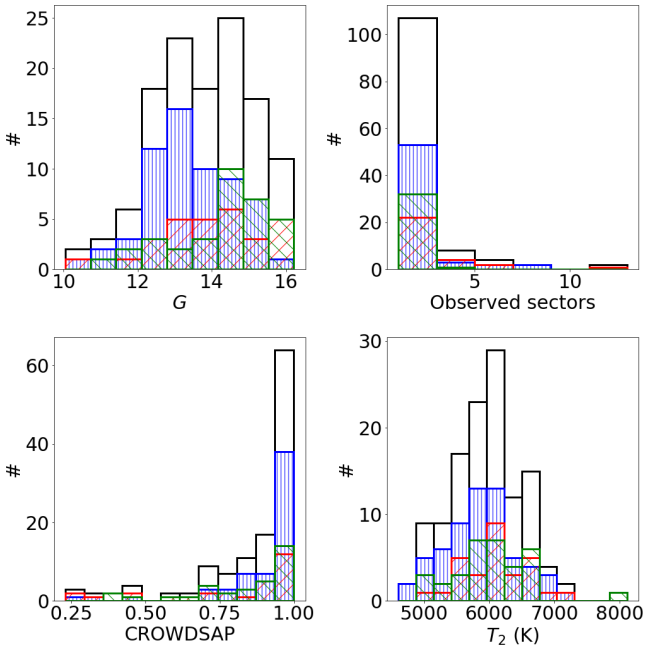

Fig. 10. Number histograms comparing the distribution of *Gaia* G magnitude (top left), TESS observed number of sectors (top right) and CROWDSAP parameter (bottom left), and companion effective temperature (bottom right) between the whole sample of 123 composites (unfilled, black), 61 rotational variables (||, blue), 33 NOV systems (\\, green), and 29 other variable systems (//, red). As these 29 systems seen to follow the distribution of the entire sample, they are excluded from our statistical analysis.

To minimise these factors, we estimate the fraction of composite stars with evidence for interaction considering only objects brighter than G = 13.5 and with CROWDSAP $\leq$ 0.97. In this case there are 26 systems, out of 21 are consistent with rotational variables. This yields a fraction of $77.8^{+5.9}_{-9.8}$%. For a confidence interval of 99.7% (3σ), the fraction is as high as 93% (see Fig. 11). For the six systems brighter than G = 12.0, the fraction of rotational variables is 100%.

Our search for common proper motion companions has resulted in 16 candidates, with projected orbital distances ranging from 2350 to 18 300 AU. Considering that 2 938 stars in our sample have passed the good astrometry criteria, this suggests that only an extremely small fraction of hot subdwarf stars are in very wide binaries. Among the progenitors, the fraction of wide binaries is around 15% (Zapatero Osorio & Martín 2004; Raghavan et al. 2010; Moe & Di Stefano 2017; Moe et al. 2019). As the fraction is much smaller for hot subdwarfs, this suggests that they cannot easily be formed in these non-interacting systems, and therefore they would also not be expected to form from single stars.

Note also that for six objects there is evidence of an inner binary companion, suggesting that these systems are rather hi-

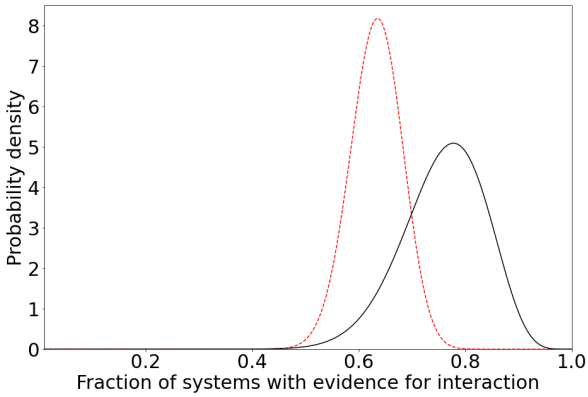

Fig. 11. Probability density for the fraction of composite systems showing evidence for interaction. The black solid line assumes the reduced sample, excluding stars that are faint and/or in crowded regions. The red dashed line assumes the whole sample.

erarchical triples. For the progenitors, El-Badry & Rix (2018) have found that, for 36% of common proper motion pairs in the main sequence, at least one of the components is a close binary. Combining this with a wide binary fraction of 15% would suggest a rate of 5.4% hierarchical triples for progenitor systems. According to Moe & Di Stefano (2017), the fraction of triple and quadruple systems for solar-type stars is 10 ± 2%. The real fraction of triple or multiple systems is unknown for our systems, because no comprehensive search for close companions has been performed for most of them, but the high fraction among the progenitors suggests that the few detected common proper motion pairs could be the progeny of triples, where the inner binary gave origin to the hot subdwarf through one of the canonical binary interaction channels.

5. Conclusion

We find that (i) the fraction of hot subdwarfs in composite binaries in which there is evidence for past interaction is higher than 60%, and can approach 100% when detection limits are taken into account, and (ii) only an extremely small number of hot subdwarfs (16 out of 2 938) could be part of a common proper motion pair. We interpret this as a strong evidence against the formation of hot subdwarf stars in single systems, and conclude that binary interaction is in fact always required.

Binary evolution scenarios must, therefore, also explain currently single objects. The merger of two He white dwarfs is one possible channel, although the agreement between observation and model predictions is still poor. The scenario proposed by de Marchi & Paresce (1996), in which envelope stripping is caused by dynamical processes, would disrupt wide binaries and thus, in principle, also produce single hot subdwarfs with no common proper motion companions. However, the scenario has been proposed for dense globular clusters and would not work for field stars. A promising alternative is offered by the scenario proposed by Clausen & Wade (2011), in which single hot subdwarfs form from the merger of a He white dwarf with a hydrogen-burning star. This scenario seems to be able to better explain the observed rotation rates and mass distribution.

It must be noted, however, that the observed mass distribution of sdO/Bs is still a work-in-progress, as they have historically been assumed to be have masses equal to the canonical He-core flash value of around 0.5 $M_\odot$ (Heber 1986; Saffer et al. 1994). Moreover, the apparent lack of companions could be explained by other factors, such as low-mass companions, which can be difficult to detect (Nelemans 2010), and observational effects, such as orbital inclination. The possible shortage of progenitors is also not established, since surveys for He-core white dwarfs are still ongoing and the population is growing (Pelisoli & Vos 2019; Brown et al. 2020; Kosakowski et al. 2020). Moreover, alternative non-single formation scenarios must be considered as well, such as supernova stripping (Justham et al. 2009), the merger of cataclysmic variables and AM CVn systems (Nelemans 2005; Zorotovic & Schreiber 2017), or interaction with sub-stellar companions (Soker 1998). Upcoming large spectroscopic surveys which will allow precise radial velocity measurements for hot subdwarfs (e.g. 4MOST, de Jong et al. 2014) will provide a better insight onto the true fraction of currently single sdO/Bs, as well as onto the observed density of possible progenitors, and further constrain the possible formation scenarios of sdO/Bs.

Acknowledgements. We thank Sydney Barnes for an enlightening discussion on stellar rotation that helped motivate this manuscript. IP was partially funded by the Deutsche Forschungsgemeinschaft under grant GE2506/12-1. This work was supported by a fellowship for postdoctoral researchers from the Alexander von Humboldt Foundation awarded to JV. This paper includes data collected by the TESS mission. Funding for the TESS mission is provided by the NASA Explorer Program. This work has made use of data from the European Space Agency (ESA) mission *Gaia* (`https://www.cosmos.esa.int/gaia`), processed by the *Gaia* Data Processing and Analysis Consortium (DPAC, `https://www.cosmos.esa.int/web/gaia/dpac/consortium`). Funding for the DPAC has been provided by national institutions, in particular the institutions participating in the *Gaia* Multilateral Agreement.

References

Andrews, J. J., Chanamé, J., & Agüeros, M. A. 2017, MNRAS, 472, 675
Baran, A., Oreiro, R., Pigulski, A., et al. 2009, MNRAS, 392, 1092
Baran, A. S., Reed, M. D., Stello, D., et al. 2012, MNRAS, 424, 2686
Barlow, B. N., Liss, S. E., Wade, R. A., & Green, E. M. 2013, ApJ, 771, 23
Barlow, B. N., Wade, R. A., Liss, S. E., Østensen, R. H., & Van Winckel, H. 2012, ApJ, 758, 58
Basri, G. & Nguyen, H. T. 2018, ApJ, 863, 190
Brown, W. R., Kilic, M., Kosakowski, A., et al. 2020, ApJ, 889, 49
Burgasser, A. J., Kirkpatrick, J. D., Reid, I. N., et al. 2003, ApJ, 586, 512
Charpinet, S., Brassard, P., Fontaine, G., et al. 2009, in American Institute of Physics Conference Series, Vol. 1170, American Institute of Physics Conference Series, ed. J. A. Guzik & P. A. Bradley, 585–596
Chen, X., Han, Z., Deca, J., & Podsiadlowski, P. 2013, MNRAS, 434, 186
Clausen, D. & Wade, R. A. 2011, ApJ, 733, L42
Copperwheat, C. M., Morales-Rueda, L., Marsh, T. R., Maxted, P. F. L., & Heber, U. 2011, MNRAS, 415, 1381
Cutri, R. M. & et al. 2012, VizieR Online Data Catalog, 2311
Davenport, J. R. A., Covey, K. R., Clarke, R. W., et al. 2019, ApJ, 871, 241
D'Cruz, N. L., Dorman, B., Rood, R. T., & O'Connell, R. W. 1996, ApJ, 466, 359
de Jong, R. S., Barden, S., Bellido-Tirado, O., et al. 2014, in Proc. SPIE, Vol. 9147, Ground-based and Airborne Instrumentation for Astronomy V, 91470M
de Marchi, G. & Paresce, F. 1996, ApJ, 467, 658
De Rosa, R. J., Patience, J., Wilson, P. A., et al. 2014, MNRAS, 437, 1216
Deca, J., Marsh, T. R., Østensen, R. H., et al. 2012, MNRAS, 421, 2798
Drilling, J. S., Jeffery, C. S., Heber, U., Moehler, S., & Napiwotzki, R. 2013, A&A, 551, A31
Duchêne, G. & Kraus, A. 2013, ARA&A, 51, 269
El-Badry, K. & Rix, H.-W. 2018, MNRAS, 480, 4884
El-Badry, K. & Rix, H.-W. 2019, MNRAS, 482, L139
Evans, D. W., Riello, M., De Angeli, F., et al. 2018, A&A, 616, A4
Fouesneau, M., Rix, H.-W., von Hippel, T., Hogg, D. W., & Tian, H. 2019, ApJ, 870, 9
Gaia Collaboration, Brown, A. G. A., Vallenari, A., et al. 2018, A&A, 616, A1
Geier, S. 2020, arXiv e-prints, arXiv:2002.10896
Geier, S., Classen, L., & Heber, U. 2011a, ApJ, 733, L13
Geier, S., Fürst, F., Ziegerer, E., et al. 2015, Science, 347, 1126
Geier, S. & Heber, U. 2012, A&A, 543, A149

Geier, S., Heber, U., Heuser, C., et al. 2013, A&A, 551, L4
Geier, S., Hirsch, H., Tillich, A., et al. 2011b, A&A, 530, A28
Geier, S., Østensen, R. H., Nemeth, P., et al. 2017, A&A, 600, A50
Geier, S., Raddi, R., Gentile Fusillo, N. P., & Marsh, T. R. 2019, A&A, 621, A38
Green, E. M., Fontaine, G., Reed, M. D., et al. 2003, ApJ, 583, L31
Han, Z., Podsiadlowski, P., Maxted, P. F. L., & Marsh, T. R. 2003, MNRAS, 341, 669
Han, Z., Podsiadlowski, P., Maxted, P. F. L., Marsh, T. R., & Ivanova, N. 2002, MNRAS, 336, 449
Heber, U. 1986, A&A, 155, 33
Heber, U. 2016, PASP, 128, 082001
Heber, U., Moehler, S., Napiwotzki, R., Thejll, P., & Green, E. M. 2002, A&A, 383, 938
Henden, A. A., Levine, S., Terrell, D., & Welch, D. L. 2015, in American Astronomical Society Meeting Abstracts, Vol. 225, American Astronomical Society Meeting Abstracts #225, 336.16
Howell, S. B., Sobeck, C., Haas, M., et al. 2014, PASP, 126, 398
Humason, M. L. & Zwicky, F. 1947, Contributions from the Mount Wilson Observatory / Carnegie Institution of Washington, 724, 1
Justham, S., Wolf, C., Podsiadlowski, P., & Han, Z. 2009, A&A, 493, 1081
Kilkenny, D., O'Donoghue, D., Koen, C., Stobie, R. S., & Chen, A. 1997, MNRAS, 287, 867
Kippenhahn, R. & Meyer-Hofmeister, E. 1977, A&A, 54, 539
Kosakowski, A., Kilic, M., Brown, W. R., & Gianninas, A. 2020, arXiv e-prints, arXiv:2004.04202
Kupfer, T., Korol, V., Shah, S., et al. 2018, MNRAS, 480, 302
Kurucz, R. L. 1979, ApJS, 40, 1
Lallement, R., Babusiaux, C., Vergely, J. L., et al. 2019, A&A, 625, A135
Latour, M., Randall, S. K., Calamida, A., Geier, S., & Moehler, S. 2018, A&A, 618, A15
Lenz, P. & Breger, M. 2005, Communications in Asteroseismology, 146, 53
Lindegren, L., Hernández, J., Bombrun, A., et al. 2018, A&A, 616, A2
Lomb, N. R. 1976, Ap&SS, 39, 447
Maxted, P. F. L., Heber, U., Marsh, T. R., & North, R. C. 2001, MNRAS, 326, 1391
Maxted, P. F. L., Marsh, T. R., & North, R. C. 2000, MNRAS, 317, L41
McNamara, B. J., Jackiewicz, J., & McKeever, J. 2012, AJ, 143, 101
Moe, M. & Di Stefano, R. 2017, ApJS, 230, 15
Moe, M., Kratter, K. M., & Badenes, C. 2019, ApJ, 875, 61
Morales-Rueda, L., Maxted, P. F. L., Marsh, T. R., North, R. C., & Heber, U. 2003, MNRAS, 338, 752
Nelemans, G. 2005, Astronomical Society of the Pacific Conference Series, Vol. 330, AM CVn stars, ed. J. M. Hameury & J. P. Lasota, 27
Nelemans, G. 2010, Ap&SS, 329, 25
Németh, P., Kawka, A., & Vennes, S. 2012, MNRAS, 427, 2180
O'Connell, R. W. 1999, ARA&A, 37, 603
Østensen, R. H., Silvotti, R., Charpinet, S., et al. 2010, MNRAS, 409, 1470
Pablo, H., Kawaler, S. D., Reed, M. D., et al. 2012, MNRAS, 422, 1343
Pelisoli, I. & Vos, J. 2019, MNRAS, 488, 2892
Popham, R. & Narayan, R. 1991, ApJ, 370, 604
Raghavan, D., McAlister, H. A., Henry, T. J., et al. 2010, ApJS, 190, 1
Reed, M. D., Foster, H., Telting, J. H., et al. 2014, MNRAS, 440, 3809
Reinhold, T. & Gizon, L. 2015, A&A, 583, A65
Reinhold, T. & Hekker, S. 2020, A&A, 635, A43
Reinhold, T. & Reiners, A. 2013, A&A, 557, A11
Retterer, J. M. & King, I. R. 1982, ApJ, 254, 214
Ricker, G. R., Winn, J. N., Vanderspek, R., et al. 2015, Journal of Astronomical Telescopes, Instruments, and Systems, 1, 014003
Riello, M., De Angeli, F., Evans, D. W., et al. 2018, A&A, 616, A3
Saffer, R. A., Bergeron, P., Koester, D., & Liebert, J. 1994, ApJ, 432, 351
Saffer, R. A., Livio, M., & Yungelson, L. R. 1998, ApJ, 502, 394
Scargle, J. D. 1982, ApJ, 263, 835
Schneider, D., Heber, U., Geier, S., Latour, M., & Irrgang, A. 2019, Fundamental Parameters of Hot Subdwarf Stars from Gaia Astrometry
Silvotti, R., Solheim, J. E., Gonzalez Perez, J. M., et al. 2000, A&A, 359, 1068
Skrutskie, M. F., Cutri, R. M., Stiening, R., et al. 2006, AJ, 131, 1163
Soker, N. 1998, AJ, 116, 1308
Stark, M. A. & Wade, R. A. 2003, AJ, 126, 1455
Sweigart, A. V. 1997, ApJ, 474, L23
Tillich, A., Heber, U., Geier, S., et al. 2011, A&A, 527, A137
Toonen, S., Nelemans, G., & Portegies Zwart, S. 2012, A&A, 546, A70
Vos, J., Bobrick, A., & Vuckovic, M. 2020, arXiv e-prints, arXiv:2003.05665
Vos, J., Németh, P., Vučković, M., Østensen, R., & Parsons, S. 2018a, MNRAS, 473, 693
Vos, J., Østensen, R. H., Degroote, P., et al. 2012, A&A, 548, A6
Vos, J., Østensen, R. H., Németh, P., et al. 2013, A&A, 559, A54
Vos, J., Østensen, R. H., Vučković, M., & Van Winckel, H. 2017, A&A, 605, A109
Vos, J., Zorotovic, M., Vučković, M., Schreiber, M. R., & Østensen, R. 2018b, MNRAS, 477, L40
Weinberg, M. D., Shapiro, S. L., & Wasserman, I. 1987, ApJ, 312, 367
Werner, K., Deetjen, J. L., Dreizler, S., et al. 2003, in ASPCS, Vol. 288, Stellar Atmosphere Modeling, ed. I. Hubeny, D. Mihalas, & K. Werner, 31
Zapatero Osorio, M. R. & Martín, E. L. 2004, A&A, 419, 167
Zhang, X., Chen, X., & Han, Z. 2009, A&A, 504, L13
Zhao, G., Zhao, Y., Chu, Y., Jing, Y., & Deng, L. 2012, arXiv e-prints, arXiv:1206.3569
Zorotovic, M. & Schreiber, M. R. 2017, MNRAS, 466, L63

Table 1. The 61 variables in our sample whose variability was attributed to rotation of the main sequence companion, identified by their TESS Input Catalogue (TIC) numbers. G is the magnitude in the *Gaia* DR2 catalogue, and the value of `CROWDSAP` is the one calculated by the SPOC pipeline. For objects with data from more than one sector, this is the averaged value. Period and amplitude uncertainties were determined with a hundred Monte-Carlo runs of the multi-component fit to the light curve, re-drawing the fluxes from a normal distribution taking the quoted uncertainties into account. The FAP was calculated using the `astropy` `LombScargle` function. $T_{\rm eff}$ and radius for the main sequence companion were obtained from a SED fit, as described in the text.

TIC	G	CROWDSAP	P (days)	Amplitude (%)	FAP	$T_{\rm eff}^{\rm MS}$ (K)	R^{MS} ($R_\odot$)
3990402	11.08	0.98	3.58050(0.00233)	0.317(0.002)	0.00e+00	5794(78)	1.14(0.06)
12528447	12.50	1.00	0.67138(0.00009)	0.334(0.005)	0.00e+00	6719(162)	1.61(0.06)
16876025	12.86	1.00	2.32635(0.00673)	0.205(0.008)	0.00e+00	6172(72)	1.27(0.07)
30019744	12.12	0.71	2.11295(0.01140)	0.163(0.007)	0.00e+00	5757(25)	1.57(0.06)
32556882	13.82	0.80	5.35140(0.05224)	0.454(0.028)	0.00e+00	5327(19)	1.22(0.05)
33526769	12.24	0.99	2.22848(0.00411)	0.147(0.004)	0.00e+00	5531(42)	0.99(0.04)
64112207	15.32	0.99	7.26000(0.16030)	0.252(0.040)	5.39e-06	5772(75)	2.10(0.26)
65263746	13.40	0.78	4.49808(0.02751)	0.171(0.010)	6.49e-72	6146(117)	0.82(0.07)
68942649	10.04	0.98	2.83832(0.00081)	0.195(0.001)	0.00e+00	6400(400)	1.10(0.05)
69841801	12.25	1.00	1.25052(0.01749)	0.883(0.137)	0.00e+00	5896(40)	1.40(0.05)
70451188	14.22	0.99	2.83560(0.01405)	0.305(0.019)	0.00e+00	5965(23)	1.28(0.06)
71248239	12.83	0.89	0.97280(0.00182)	0.173(0.009)	0.00e+00	6049(36)	1.30(0.03)
71716888	12.97	0.99	1.04908(0.00227)	0.066(0.029)	3.75e-24	6991(38)	1.62(0.08)
92865531	13.12	0.96	1.40297(0.00017)	1.888(0.007)	0.00e+00	5004(14)	1.43(0.04)
116416387	14.65	0.84	3.81890(0.03845)	0.402(0.043)	0.00e+00	5514(46)	0.99(0.06)
118269334	13.82	0.97	3.07313(0.00664)	0.717(0.019)	0.00e+00	5478(74)	0.97(0.05)
143058705	14.40	0.98	5.02699(0.03025)	0.540(0.028)	0.00e+00	5449(42)	1.00(0.06)
146323153	12.15	0.96	0.21904(0.00002)	0.199(0.003)	0.00e+00	6792(43)	1.66(0.04)
149767908	13.00	0.99	0.45568(0.00057)	0.229(0.010)	0.00e+00	7300(56)	1.67(0.12)
151641733	12.65	0.96	0.55921(0.00076)	0.028(0.005)	2.03e-10	6539(41)	1.48(0.05)
157323544	12.69	0.99	4.46196(0.04300)	0.080(0.007)	0.00e+00	6250(291)	2.41(0.10)
158335560	13.08	0.92	2.00072(0.00407)	0.244(0.013)	0.00e+00	6062(70)	1.45(0.08)
159805154	14.80	0.90	2.68552(0.00948)	0.293(0.336)	5.95e-32	5642(49)	1.50(0.23)
160583519	14.43	0.98	1.97311(0.00065)	0.175(0.011)	0.00e+00	5993(51)	1.29(0.05)
164754858	14.70	0.80	2.67902(0.02374)	0.228(0.026)	1.66e-11	5863(53)	1.87(0.26)
165650748	11.38	1.00	2.11600(0.00019)	0.077(0.002)	0.00e+00	6625(122)	1.40(0.03)
198240464	13.52	0.89	2.35724(0.00007)	0.816(0.006)	0.00e+00	5646(53)	1.19(0.02)
202466623	13.81	0.97	3.32074(0.00073)	0.237(0.011)	0.00e+00	6008(59)	1.15(0.03)
202507151	12.69	0.99	1.98289(0.00036)	0.135(0.005)	0.00e+00	6356(69)	1.03(0.03)
206688085	13.77	0.99	1.91975(0.00028)	2.337(0.009)	0.00e+00	4935(46)	2.43(0.07)
207208668	13.33	0.98	2.56713(0.00063)	0.362(0.360)	0.00e+00	6110(52)	1.17(0.04)
209397773	12.73	0.83	3.58018(0.08782)	0.084(0.054)	1.05e-69	5460(34)	1.23(0.04)
212320065	11.64	0.98	1.86265(0.00075)	1.416(0.008)	0.00e+00	5097(13)	2.50(0.00)
219988867	13.03	0.96	1.92093(0.00195)	0.101(0.004)	0.00e+00	6092(56)	1.45(0.04)
228508601	14.40	0.99	5.58009(0.05841)	0.346(0.024)	0.00e+00	5400(40)	1.97(0.33)
231845752	13.72	0.96	2.09227(0.00352)	0.088(0.008)	1.51e-31	5863(62)	1.69(0.05)
247017534	12.15	0.92	1.81542(0.00459)	0.094(0.100)	0.00e+00	5944(28)	1.35(0.05)
263014094	15.03	0.88	2.91052(0.00014)	1.531(0.025)	0.00e+00	5000(9)	1.64(0.08)
277892210	13.91	0.95	1.80779(0.00002)	1.658(0.028)	0.00e+00	5460(48)	1.23(0.03)
293463617	15.13	0.87	1.74504(0.00012)	1.337(0.040)	0.00e+00	4611(39)	0.80(0.04)
298093039	11.62	1.00	5.56099(0.00062)	0.162(0.003)	0.00e+00	5876(127)	0.90(0.02)
304103779	12.96	0.99	1.12766(0.00011)	0.060(0.005)	9.54e-37	5967(28)	1.54(0.04)
317129309	13.44	0.98	3.85836(0.12472)	1.541(2.606)	6.53e-24	6501(34)	1.83(0.14)
320529836	14.65	0.88	0.83535(0.00085)	1.839(0.130)	0.00e+00	5251(44)	0.97(0.04)
320965274	12.66	0.99	1.75852(0.00620)	0.044(0.005)	8.53e-22	5286(28)	1.80(0.11)
325566833	13.35	0.98	1.06283(0.00150)	0.069(0.007)	9.39e-23	5290(22)	1.28(0.02)
335682563	13.55	0.99	4.41730(0.00213)	0.112(0.007)	0.00e+00	5986(67)	0.94(0.03)
346597868	11.52	0.97	1.78157(0.00620)	0.032(0.003)	5.51e-28	6437(96)	2.29(0.07)
349367583	13.05	0.99	2.30160(0.01395)	0.232(0.238)	0.00e+00	5919(53)	1.46(0.05)
365771053	13.37	0.85	1.35154(0.00059)	1.089(0.014)	0.00e+00	5981(26)	1.14(0.02)
369371996	15.91	0.98	2.60612(0.00883)	0.150(0.010)	2.14e-40	5801(162)	2.34(0.14)
382518318	14.01	0.29	4.33102(0.00040)	1.402(0.025)	0.00e+00	5205(24)	1.27(0.04)
389752750	15.24	0.82	0.67638(0.00022)	0.889(0.040)	0.00e+00	4807(84)	1.34(0.30)
393941149	14.73	0.86	3.87295(0.02929)	0.364(0.025)	0.00e+00	5118(44)	1.04(0.11)
398940155	13.08	0.47	0.50387(0.00070)	0.624(0.116)	0.00e+00	6976(64)	2.10(0.14)
405471275	15.19	0.33	3.51030(0.04024)	0.422(0.059)	2.66e-12	5915(55)	1.29(0.29)

Table 1 continued.

TIC	G	CROWDSAP	P (days)	Amplitude (%)	FAP	$T_{\rm eff}^{\rm MS}$ (K)	R^{MS} ($R_\odot$)
406239686	13.45	0.98	1.63307(0.00541)	0.124(0.130)	1.16e-41	5498(31)	1.39(0.05)
420049852	12.13	0.81	1.66633(0.00713)	0.054(0.005)	6.95e-35	6312(57)	1.36(0.04)
437237493	15.36	0.72	1.26476(0.00385)	0.845(0.423)	0.00e+00	6185(60)	1.41(0.19)
441401311	13.74	0.99	2.91515(0.00587)	0.275(0.012)	0.00e+00	5740(21)	1.46(0.07)
461156754	14.96	0.74	1.61028(0.00640)	0.321(0.042)	2.32e-20	5729(58)	1.57(0.17)

Table 2. The 29 objects whose variability was not attributed to rotation. Columns are the same as in Table 1.

TIC	G	CROWDSAP	P (days)	Amplitude (%)	FAP	$T_{\rm eff}^{\rm MS}$ (K)	R^{MS} ($R_\odot$)
13069774	12.29	0.97	2.38024(0.01057)	0.058(0.028)	0.00e+00	5968(22)	1.29(0.02)
31636688	16.01	0.78	2.80557(0.01477)	0.392(0.060)	2.88e-07	6973(35)	1.62(0.37)
71013467	13.42	0.99	0.02887(0.00000)	0.011(0.002)	8.82e-17	6010(33)	1.84(0.08)
71133157	14.06	0.98	2.15624(0.01586)	0.121(0.015)	3.17e-10	6751(74)	1.31(0.07)
80057233	15.79	0.62	6.53343(0.12416)	2.981(0.434)	1.49e-14	5986(73)	1.78(0.38)
89529774	14.31	0.96	4.38034(0.05663)	0.106(0.013)	4.73e-08	5548(30)	2.41(0.09)
141628019	14.34	0.95	10.41692(0.05044)	0.060(0.009)	2.75e-38	5518(28)	2.32(0.18)
147115112	14.27	0.60	1.64319(0.01285)	0.098(0.017)	2.25e-04	6458(77)	1.60(0.12)
152374958	13.08	0.73	4.85523(0.05702)	0.093(0.011)	2.04e-28	6014(23)	2.36(0.09)
158235404	11.64	0.76	0.04989(0.00000)	0.024(0.001)	0.00e+00	6741(141)	2.35(0.10)
159669717	13.81	0.72	7.56916(0.30956)	0.071(0.049)	2.00e-07	6174(80)	1.64(0.11)
181820016	12.82	0.99	10.26284(0.44484)	0.055(0.008)	4.67e-18	6518(129)	1.48(0.08)
197693940	14.40	0.90	6.40408(0.13418)	0.249(0.040)	5.11e-12	4974(47)	0.53(0.04)
220026025	15.67	0.87	9.85020(0.06937)	18.464(10.410)	2.26e-23	5346(63)	1.77(0.66)
220472655	14.48	0.96	3.13006(0.00461)	0.078(0.010)	6.23e-18	6734(93)	1.35(0.06)
246881770	15.39	0.89	7.12875(0.09014)	0.379(0.045)	6.31e-07	5680(76)	1.27(0.18)
253932935	16.00	0.89	13.41583(1.79633)	0.292(0.469)	3.86e-17	6159(110)	1.88(0.40)
257024892	13.05	0.99	2.20766(0.00162)	0.022(0.005)	2.91e-07	6197(34)	2.20(0.07)
259963278	10.61	1.00	0.83783(0.00007)	0.009(0.001)	1.15e-24	6494(20)	1.46(0.02)
266347283	12.55	0.99	0.90114(0.00113)	0.033(0.005)	4.07e-15	6523(139)	1.42(0.04)
274035031	13.96	0.46	2.82457(0.01273)	0.090(0.016)	2.41e-07	6054(21)	1.67(0.05)
289737935	14.97	0.90	3.03006(0.03695)	0.182(0.032)	1.09e-04	5768(92)	1.46(0.22)
313303167	12.46	0.88	0.42706(0.00000)	0.775(0.005)	0.00e+00	7136(128)	1.37(0.04)
320176500	15.79	0.46	6.39116(0.38431)	0.646(0.260)	6.34e-10	6157(47)	1.88(0.38)
389520459	14.03	0.99	1.34965(0.00589)	0.092(0.013)	6.41e-06	5799(50)	2.18(0.16)
410135274	15.41	0.25	6.95850(0.07557)	0.863(0.061)	7.30e-44	5496(22)	2.04(0.25)
410390905	13.39	0.99	0.99130(0.00010)	0.061(0.005)	2.77e-33	5900(44)	1.58(0.03)
424941595	14.49	0.34	6.87997(0.18727)	0.226(0.039)	2.12e-15	5453(36)	2.50(0.00)
453366788	13.94	0.23	5.06463(0.03818)	0.285(0.029)	1.12e-33	6250(50)	1.19(0.08)

Table 3. Systems for which no variability has been detected. TIC, G, CROWDSAP, $T_{\rm eff}$ and radius are the same as in Table 1. The detection limit has been calculated as five times the average amplitude in a Fourier transform of the light curve.

TIC	G	CROWDSAP	Detection limit (%)	$T_{\rm eff}^{\rm MS}$ (K)	R^{MS} ($R_\odot$)
9102069	15.04	0.88	0.173	6010(162)	1.72(0.23)
13090700	14.73	0.99	0.125	6688(57)	1.85(0.17)
25245570	15.12	0.69	0.282	5950(82)	1.88(0.34)
32661254	11.29	0.97	0.013	6424(52)	1.74(0.07)
56648314	14.13	0.99	0.090	5770(26)	1.84(0.28)
71150825	14.61	0.66	0.126	5382(16)	1.35(0.08)
71410075	15.87	0.75	0.302	6324(150)	1.04(0.13)
98871628	14.34	0.93	0.115	5696(24)	1.13(0.07)
117626475	12.60	1.00	0.035	6161(112)	1.05(0.09)
121550523	14.32	0.92	0.109	6128(69)	1.49(0.07)
141602548	12.10	0.98	0.014	6706(171)	1.70(0.04)
146437397	13.47	0.97	0.047	5797(59)	1.63(0.05)
151892844	14.98	0.98	0.222	5047(69)	0.57(0.08)
179278778	15.07	0.86	0.307	5855(96)	2.04(0.24)
220370211	14.84	0.37	0.339	5781(70)	1.26(0.10)
248949857	12.23	1.00	0.025	6507(27)	1.82(0.14)
260839766	15.39	0.85	0.313	6064(213)	1.89(0.25)
261427146	12.07	0.95	0.021	6069(121)	1.66(0.69)
261679852	16.22	0.90	0.447	5095(63)	1.47(0.34)
281851153	14.96	0.72	0.188	6501(34)	1.83(0.14)
283866221	15.58	0.69	0.381	8117(217)	1.38(0.42)
301405970	12.57	1.00	0.031	6605(86)	2.03(0.10)
339525222	13.80	0.98	0.061	6016(26)	1.87(0.08)
362105045	15.39	0.97	0.142	6400(79)	1.05(0.10)
370282569	14.60	0.97	0.114	5845(53)	2.22(0.15)
377053047	14.82	0.45	0.148	6550(50)	1.46(0.15)
392703299	15.81	0.70	0.319	5431(108)	2.13(0.23)
394631720	14.39	0.76	0.113	5311(57)	1.29(0.07)
413300076	15.77	0.37	0.418	5116(74)	1.73(0.60)
421951567	13.90	0.88	0.079	6216(46)	2.08(0.21)
422149668	14.48	0.98	0.143	5607(62)	1.71(0.13)
436639479	14.41	0.86	0.149	6296(83)	0.77(0.05)
441399312	13.28	0.57	0.064	5499(124)	1.89(0.10)

Table 4. Identified common proper motion candidates. The four columns to the left refer to the hot subdwarf, whereas the next four refer to the candidate common proper motion companion. All values come directly from the *Gaia* DR2 catalogue. The last four columns contain pair properties, namely the angular separation θ, the projected orbital separation a, assuming the distance of the hot subdwarf, and the differences in parallax and proper motion in units of standard deviation, $\Delta\varpi$ and $\Delta\mu$. The six objects marked with asterisks have identified close companions, being therefore candidate triple systems (see Section 3.1).

Hot subdwarf					*Candidate companion*					*Pair properties*			
source_id	G (mag)	ϖ (mas)	μ_α (mas/yr)	μ_δ (mas/yr)	source_id	G (mag)	ϖ (mas)	μ_α (mas/yr)	μ_δ (mas/yr)	θ (")	a (AU)	$\Delta\varpi$	$\Delta\mu$
312628749626419328*	13.1	1.73	-8.80	-11.27	312628745331966976	18.7	1.47	-9.74	-12.16	6.8	3920	1.1	2.8
601188910547673728	14.6	0.69	-5.02	-0.80	601188910547673600	15.4	0.58	-5.15	-0.75	2.7	3856	1.6	1.3
992534888766785024*	12.0	2.93	-25.48	-25.16	992534888766784640	13.8	3.03	-25.57	-25.01	7.0	2384	1.3	1.3
1332156747638095488	15.9	0.46	-5.22	-27.03	1332156747638095360	16.7	0.65	-5.41	-27.29	4.1	8996	1.7	1.7
1659750327258228352	16.2	0.53	-1.74	-0.70	1659750327258228224	17.9	0.62	-2.02	-0.65	1.9	3595	0.7	1.3
1660055029417965952	13.4	2.18	-18.82	3.51	1660055098137442944	17.5	2.10	-18.82	3.95	39.8	18291	0.7	2.7
1883850072814402048	13.0	0.98	-1.80	-13.31	1883850072814402432	17.4	0.96	-1.59	-13.57	11.5	11655	0.2	1.9
1891098500140100352	12.8	2.11	11.43	-1.30	1891098500140101120	12.9	2.05	11.41	-1.17	26.0	12349	0.9	1.5
2002880555945732992	14.4	1.46	4.72	1.57	2002880555945731968	17.0	1.42	4.97	1.70	3.4	2346	0.4	2.2
2103959862471941632*	14.1	1.55	-0.64	-8.95	2103959858173621760	18.8	1.50	-0.74	-8.72	15.9	10253	0.2	0.6
3381286602335612416	14.0	0.60	-3.11	-7.56	3381286636695992448	17.9	1.08	-2.70	-7.16	8.5	14220	2.9	2.0
3484319745326973824*	11.3	1.95	-7.66	-23.66	3484320501241217792	16.1	1.92	-8.10	-23.65	6.4	3307	0.2	2.4
3868418219635118080*	14.2	1.08	-21.76	13.79	3868418219635275520	16.0	1.41	-21.81	13.87	8.6	8019	1.9	0.2
4491274930955326080	15.6	0.61	0.08	-10.03	4491274930955325440	16.8	0.49	0.27	-10.06	4.9	8014	1.3	1.3
4877263019073081600*	12.3	1.72	7.03	20.44	4877263023370516096	17.3	1.59	7.36	20.51	20.9	12144	1.6	2.5
1429755412672689536	13.7	1.30	-6.44	-4.82	1429755374017588608	12.6	1.43	-6.50	-4.50	3.6	2764	2.4	2.9

Appendix A: Pulsation periods for two new g-mode pulsators

Table A.1. Periods above a 5-σ detection level for the two newly identified pulsators. Pre-whitening and error estimates were performed with Period04 (Lenz & Breger 2005).

TIC 071013467 (G = 13.4)	
Period (h)	Amplitude (%)
0.69 ± 0.01	0.07 ± 0.03
1.11 ± 0.07	0.06 ± 0.02
0.87 ± 0.06	0.05 ± 0.02
TIC 158235404 (G = 11.6)	
Period (h)	Amplitude (%)
1.19729 ± 0.00003	0.113 ± 0.003
1.5057 ± 0.0001	0.040 ± 0.003

Appendix B: ADQL query for co-moving sources within 20 000 AU

```
SELECT sd.NAME, sd.source_id, sd.ra, sd.dec, sd.parallax, sd.parallax_error,
       sd.pmra, sd.pmdec, sd.pmra_error, sd.pmdec_error,
       g.source_id, g.ra, g.dec, g.parallax, g.parallax_error,
       g.pmra, g.pmra_error, g.pmdec, g.pmdec_error,
       g.phot_g_mean_mag, g.bp_rp, g.phot_bp_rp_excess_factor,
       g.astrometric_chi2_al, g.astrometric_n_good_obs_al,
       DISTANCE(POINT('ICRS', sd.ra, sd.dec), POINT('ICRS', g.ra, g.dec)) AS dist
FROM [INPUT TABLE] AS sd
JOIN gaiadr2.gaia_source AS g
ON 1=CONTAINS(POINT('ICRS', sd.ra, sd.dec), CIRCLE('ICRS', g.ra, g.dec, 20.0*sd.parallax/3600.))
WHERE (sd.source_id != g.source_id)
AND ( ( (sd.pmra - g.pmra)*(sd.pmra - g.pmra)/
(sd.pmra_error*sd.pmra_error + g.pmra_error*g.pmra_error) +
(sd.pmdec - g.pmdec)*(sd.pmdec - g.pmdec)/
(sd.pmdec_error*sd.pmdec_error + g.pmdec_error*g.pmdec_error) ) <= 9.0 )
AND ( (sd.parallax - g.parallax)*(sd.parallax - g.parallax)/
(sd.parallax_error*sd.parallax_error + g.parallax_error*g.parallax_error) <= 9.0 )
```